



## ISTITUTO NAZIONALE DI RICERCA METROLOGICA Repository Istituzionale

Design optimization through thermomechanical finite-element analysis of a hybrid piston-clamped anvil cell for nuclear magnetic resonance experiments

*Original*

Design optimization through thermomechanical finite-element analysis of a hybrid piston-clamped anvil cell for nuclear magnetic resonance experiments / Barbero, N.; Abbiati, G.; Enrico, E.; Amato, G.; Vittone, E.; Ott, H. -R.; Mesot, J.; Shiroka, T.. - In: REVIEW OF SCIENTIFIC INSTRUMENTS. - ISSN 0034-6748. - (2019). [10.1063/1.5059391]

*Availability:*

This version is available at: 11696/65898 since: 2021-01-29T13:57:03Z

*Publisher:*

American Institute of Physics

*Published*

DOI:10.1063/1.5059391

*Terms of use:*

This article is made available under terms and conditions as specified in the corresponding bibliographic description in the repository

*Publisher copyright*

(Article begins on next page)

# Design optimization through thermomechanical finite-element analysis of a hybrid piston-clamped anvil cell for nuclear magnetic resonance experiments

Cite as: Rev. Sci. Instrum. **90**, 013901 (2019); <https://doi.org/10.1063/1.5059391>

Submitted: 20 September 2018 . Accepted: 14 December 2018 . Published Online: 03 January 2019

 N. Barbero,  G. Abbiati, E. Enrico, G. Amato,  E. Vittone, H.-R. Ott, J. Mesot, and  T. Shiroka



View Online



Export Citation



CrossMark

## ARTICLES YOU MAY BE INTERESTED IN

### [A single-chip integrated transceiver for high field NMR magnetometry](#)

Review of Scientific Instruments **90**, 015001 (2019); <https://doi.org/10.1063/1.5066436>

### [Parameter estimation of linear frequency modulation signals based on sampling theorem and fractional broadening](#)

Review of Scientific Instruments **90**, 014702 (2019); <https://doi.org/10.1063/1.5041031>

### [Design and analysis of a burst strength device for testing vascular grafts](#)

Review of Scientific Instruments **90**, 014301 (2019); <https://doi.org/10.1063/1.5037578>



New

## Your Qubits. Measured.

Meet the next generation of quantum analyzers

- Readout for up to 64 qubits
- Operation at up to 8.5 GHz, mixer-calibration-free
- Signal optimization with minimal latency

Find out more


# Design optimization through thermomechanical finite-element analysis of a hybrid piston-clamped anvil cell for nuclear magnetic resonance experiments

Cite as: Rev. Sci. Instrum. 90, 013901 (2019); doi: 10.1063/1.5059391

Submitted: 20 September 2018 • Accepted: 14 December 2018 •

Published Online: 3 January 2019



View Online



Export Citation



CrossMark

N. Barbero,<sup>1,a)</sup>  G. Abbiati,<sup>2</sup>  E. Enrico,<sup>3</sup> G. Amato,<sup>3,4</sup> E. Vittone,<sup>5</sup>  H.-R. Ott,<sup>1,6</sup> J. Mesot,<sup>1,6</sup> and T. Shiroka<sup>1,6</sup> 

## AFFILIATIONS

<sup>1</sup>Laboratorium für Festkörperphysik, ETH Zürich, CH-8093 Zurich, Switzerland

<sup>2</sup>Department of Civil, Environmental and Geomatic Engineering, ETH Zürich, CH-8093 Zurich, Switzerland

<sup>3</sup>Nanoscience and Materials Division, INRIM, Strada delle Cacce 91, Turin, Italy

<sup>4</sup>Dipartimento Scienze and Innovazione Tecnologica, Università del Piemonte Orientale, 1512 Alessandria, Italy

<sup>5</sup>Physics Department and NIS Interdepartmental Center, University of Torino, Via Pietro Giuria 1, 10125 Torino, Italy

<sup>6</sup>Paul Scherrer Institute, CH-5232 Villigen PSI, Switzerland

<sup>a)</sup>Electronic mail: [nbarbero@phys.ethz.ch](mailto:nbarbero@phys.ethz.ch)

## ABSTRACT

The investigation of materials under extreme pressure conditions requires high-performance cells whose design invariably involves trade-offs between the maximum achievable pressure, the allowed sample volume, and the possibility of real-time pressure monitoring. With a newly conceived hybrid piston-clamped anvil cell, we offer a relatively simple and versatile system, suitable for nuclear magnetic resonance experiments up to 4.4 GPa. Finite-element models, taking into account mechanical and thermal conditions, were used to optimize and validate the design prior to the realization of the device. Cell body and gaskets were made of beryllium-copper alloy and the pistons and pusher were made of tungsten carbide, while the anvils consist of zirconium dioxide. The low-temperature pressure cell performance was tested by monitoring *in situ* the pressure-dependent <sup>63</sup>Cu nuclear-quadrupole-resonance signal of Cu<sub>2</sub>O.

Published under license by AIP Publishing. <https://doi.org/10.1063/1.5059391>

## I. INTRODUCTION

Pressure is a versatile parameter to reversibly tune the structural and electronic properties of numerous types of materials, as well as to explore their phase diagrams.<sup>1</sup> From 1960s up to present, a large number of studies have shown that pressure can induce or significantly affect superconductivity and/or magnetic order of both simple and complex materials. For example, elemental cerium<sup>2</sup> or MnP<sup>3</sup> adopt a magnetically ordered ground state at ambient pressure but turn into superconductors at 5 and 8 GPa, respectively. More recently, theoretical calculations<sup>4–6</sup> suggested that, in magnetically frustrated and strongly spin-orbit coupled oxides, external pressure may induce a quantum-spin-liquid

state, thus triggering a flurry of experimental studies of compounds such as  $\alpha$ -RuCl<sub>3</sub>,<sup>7</sup> the  $\alpha$ - and  $\beta$ -phases of Li<sub>2</sub>IrO<sub>3</sub>,<sup>8,9</sup> and Na<sub>2</sub>IrO<sub>3</sub>.<sup>10</sup> Finally, pressure plays a significant role in the attempts to achieve room-temperature superconductivity. In particular, pressure-induced metallization and superconductivity were reported in hydrogen-based materials, such as H<sub>3</sub>S<sup>11</sup> and LaH<sub>10</sub>,<sup>12</sup> the latter exhibiting a remarkable T<sub>c</sub> of 215 K.<sup>13</sup> From the technical perspective, record pressures up to 1400 GPa were achieved to investigate the high-pressure properties of diamond.<sup>14</sup>

The design of efficient pressure cells is always a challenging task.<sup>15</sup> The most intuitive layout of a piston-clamped device, even using the most appropriate materials, such as

beryllium-copper (BeCu), NiCrAl, and MP35N alloy (35% Ni, 35% Co, 20% Cr, and 10% Mo), exhibits an upper pressure limit  $p_{cr}$  of 3 GPa.<sup>15</sup> To overcome this limit, double-wall piston-clamped systems were developed, for instance, with a NiCrAl inner body and a BeCu outer sleeve. Yet, the intrinsic mechanical properties of the used materials still do not allow pressure values above 4 GPa.<sup>16</sup> Higher pressure regimes can be achieved through a different design, resulting in severe restrictions to the size of the sample to be investigated. A more sophisticated approach, which uses anvil cells to reach higher pressures, was pioneered by Bridgman more than 100 years ago.<sup>17</sup> In this design, two anvils, typically with the shape of truncated cones, squeeze a gasket containing the sample and a suitable pressure-transmitting medium. Although higher pressures substantially exceeding  $p_{cr}$  can be achieved, the allowed sample size is severely reduced. For both designs, adaptations to cope with additional requirements, such as direct electrical contacts or optical access, are possible. Simple contacts for measuring the electrical conductivity up to 40 GPa may be implemented without major difficulties in a Bridgman cell.<sup>18</sup> Optical access is achieved by employing diamond anvils, and gaskets with holes, with diameters varying from 1 mm to 1  $\mu\text{m}$ .<sup>15</sup> More demanding requirements arise when additional components have to be installed inside the sample space, i.e., in the hole of the gasket, such as radio-frequency (RF) micro-coils for nuclear magnetic resonance (NMR) experiments. In early attempts of this kind, the necessary coil or split coil was wound around the anvils and the gasket, thus allowing measurements at pressures up to 5.2 and 8.3 GPa.<sup>19,20</sup> In this configuration, the obvious drawback is a low filling factor and, hence, a poor signal-to-noise ratio (SNR). More recently, NMR studies up to 10 GPa could be performed using NiCrAl-based pressure cells, with a design that locates the RF micro-coil inside the bore of the gasket and an additional loading setup which uses argon as a pressure-transmitting medium.<sup>21–23</sup> Finally, with technically very demanding solutions, including composite gaskets and Lenz electromagnetic lenses in toroidal diamond-indenter cells, record pressures up to 90 GPa could be achieved.<sup>24–26</sup>

In this paper, we describe the design and testing of a relatively simple and versatile pressure cell, suitable for NMR experiments up to 4.4 GPa. The distinguishing feature of our approach is the use of thermomechanical analyses to optimize the piston-clamped anvil-cell design by means of detailed calculations of deformation, stress, and strain. To reach pressures above  $p_{cr}$ , the realized solution employs the strength of piston-clamped systems augmented by the anvil-based technology. In order to enhance the SNR, and thus utilize also less-sensitive nuclei as local probes, we place the micro-coil inside the tiny sample space.

To validate the design, a 3D geometrical model of the pressure cell was developed with Autodesk Inventor<sup>®</sup>, a widely used 3D computer-aided design (CAD) tool. The thermomechanical response of the cell was simulated through finite-element analysis (FEA) using the ANSYS<sup>®</sup> software. The simulations allowed us to control the plastic deformations

of the anvil-gasket system, to optimize the dimensions of key components, and to avoid significant deformations of the internal RF micro-coil.

To monitor the pressure *in situ*, most of the current designs employ the ruby-fluorescence method.<sup>27</sup> Despite its accuracy, this imposes the use of optically transparent (diamond) anvils. In our design, instead, the pressure is monitored via the <sup>63</sup>Cu nuclear-quadrupole-resonance (NQR) signal of Cu<sub>2</sub>O.<sup>28,29</sup> This choice has the advantage of using ZrO<sub>2</sub> anvils, more easily obtained commercially and less expensive than diamond, while still providing a high compressive-yield strength.

## II. DESIGN AND TECHNOLOGY OF THE HYBRID PRESSURE CELL

### A. Cell design and preparation

The hybrid piston-clamped anvil cell, shown in Fig. 1, consists of a system, whose body and locknuts are made of hardened BeCu alloy (at 315 °C, for 3 h, in argon atmosphere) to increase the yield strength. The tungsten carbide (WC) pusher has a circular cross section with a 10-mm diameter. Once the pusher is loaded with a force varying between 0 and 20 kN, the piston is clamped by tightening the body-locknut screw, which holds the pre-loading force. Two anvils made of ZrO<sub>2</sub>, a material with excellent compressive strength, are connected to the relevant locknuts by WC pistons. Under



**FIG. 1.** Main components of the hybrid piston-clamped anvil cell. The pusher (1), made of WC, is used to load the cell. The body assembly and the upper and lower cell locknuts (2) are made of age-hardened BeCu alloy (Berylico25<sup>®</sup>). The hole in the longitudinal center of the body is used to fix the sample-gasket thermometer and to inspect the correct alignment of the gasket during the loading. (3) and (4) are two (non age-hardened) BeCu gaskets 0.8-mm thick resting on their respective centering supports made of Teflon. We chose three different hole sizes: small (0.4 mm), intermediate (0.8 mm), and large (1.4 mm), of which the latter two are shown. (5) Assembly of the top anvil and piston made of zirconium dioxide and tungsten carbide, respectively. (6) Assembly of the bottom anvil and piston. Four sputtered gold contacts are visible on the surface of the anvil, allowing the use of the pressure cell without a feedthrough (one of the two possible variants).

applied force, the anvils notch the BeCu gasket, with the notch footprints matching the indenting anvil, whose diameters vary between 1.2 and 4 mm. Finally, the BeCu gasket compresses the pressure-transmitting medium (Daphne oil 7575) in which the sample is immersed. Gaskets are provided with holes of different internal diameters (0.4, 0.8, and 1.4 mm) and are aligned to the 16-mm cell bore by means of a sliding fit (tolerance  $g6/H7$ ) and a centering gasket-holder made of Teflon<sup>®</sup>, the latter being fixed to the lower anvil. The correct gasket alignment and locking are crucial to achieving high pressures. An improved version of our setup may include a self-aligning gasket-anvil system, similar to the Boehler-Almax design.<sup>30</sup> The control of the sample temperature is achieved by adjusting a helium flow, here acting as a cryogenic fluid, and an electric heater glued on the outer surface of the cell body, close to the inspection hole. A schematic representation of the main components of the cell is presented in Fig. 2.

As for the electrical contacts to the RF coil, we devised two different configurations, in order to compare the performance of the layered contact vs. the feedthrough method for contacting the leads. The first is based on sputtering gold contacts onto the bottom anvil [see Fig. 3(a)], while the second requires drilling of a tapered hole in the bottom anvil, acting as a feedthrough for the leads [see Fig. 3(b)]. In the first

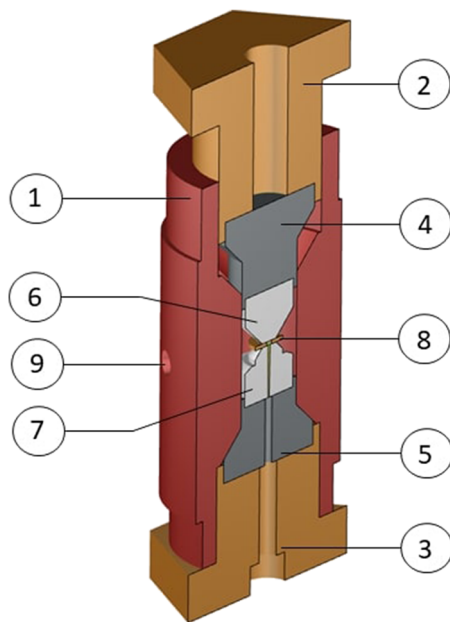


**FIG. 2.** Drawing of the pressure cell assembly. (1) Body of the pressure cell in age-hardened BeCu. (2) Upper locknut of the pressure cell with a 10-mm bore for the pusher (sliding fit precision required). (3) Lower locknut of the pressure cell with a 5-mm feedthrough for the leads. (4) WC top piston. (5) WC bottom piston with a feedthrough of 2 mm of diameter. (6) Upper ZrO<sub>2</sub> anvil. (7) Lower ZrO<sub>2</sub> anvil with a tapered bore, reduced from the outer 600 to the inner 300 nm in diameter, used for the second configuration of the cell. The bore is sealed with Stycast 2850 FT<sup>®</sup> epoxy mixed with diamond powder. (8) BeCu gasket. (9) Hole for gasket inspection and thermometer installation.

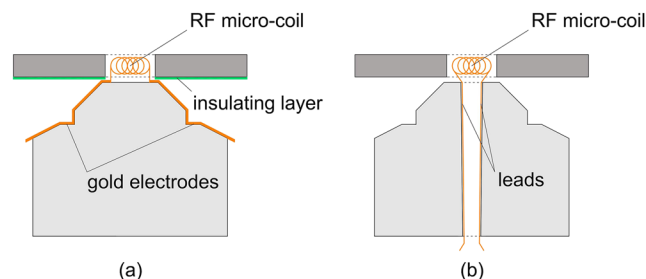


**FIG. 3.** Two possible configurations for transmitting the electrical signals to and from the RF micro-coil: (a) without and (b) with a feedthrough. In (a), coil leads are glued with conductive silver epoxy to the gold electrodes sputtered on the surface of the lower anvil. A thin Al<sub>2</sub>O<sub>3</sub> layer insulates the lower side of the gasket. In (b), coil leads pass through a tapered hole in the lower anvil. For clarity, geometric proportions have not been preserved, in particular, those of the gasket and of the RF micro-coil.

case, the bottom face of the gasket is protected by an insulating 1- $\mu\text{m}$ -thick Al<sub>2</sub>O<sub>3</sub> layer, which avoids short-circuits among the four triangular-shaped 0.4- $\mu\text{m}$ -thick gold contacts. Once the photolithographic mask was drawn to define the electrodes, the gasket surface was exposed to gold sputtering and then cleaned by sonication in an acetone bath. The resulting contacts are clearly delicate, but gold is regarded as one of the best options, both due to its wear performance and to its increased contact area under stress.<sup>15,31</sup> The RF micro-coil was then glued to the gold contacts using conductive silver epoxy. Recently, an alternative configuration was proposed, based on the so-called *designer* anvil, an anvil featuring a metallic micro-channel located in its culet.<sup>32</sup>

Our second design employs a bottom anvil with a tapered hole [narrowing from the top to bottom from 600 to 300 nm, see Fig. 3(b)] for the leads that transmit the RF pulses and the NMR signal to and from the coil. In this variant, after the introduction of the leads, the tapered hole is sealed with Stycast 2850 FT epoxy mixed with fine diamond powder. This second solution proved less delicate during cell preparation and loading, although both configurations exhibit a non-negligible failure rate. In the first case, this is due to the delicate contacts between the micro-coil wires and the gold pads and to possible damaging of the latter during cell loading. The second configuration is fairly robust but, besides a longer preparation time, the coil wires can still be damaged during the loading protocol and, due to the difficulties in removing the epoxy resin used to seal the tapered hole, the lower anvil can be used only once.

We performed four test runs with the first- and six test runs with the second configuration, obtaining two and four failures during cell loading, respectively. A high failure rate is typical of these kinds of experiments, yet future improved designs are expected to lower the failure rate by making the cell loading more practical.

The micro-coils (Shannon MicroCoil), located inside the hole of the gasket, were fabricated by winding insulated copper wires with a cross section of 30  $\mu\text{m}$ . Considering the

**TABLE I.** Key material properties at 293 K (room temperature).  $E$  = Young's modulus;  $\nu$  = Poisson's ratio;  $\sigma_y$  = scalar von Mises stress;  $\rho$  = density;  $\alpha$  = thermal expansion coefficient;  $\kappa_T$  = thermal conductivity;  $c$  = specific heat. At low temperature (10 K), only Beryllco25 and its age-hardened version show a 10% increase of  $E$ , as well as an increase of 11% and 3% of  $\sigma_y$ , respectively.

Material	Component	$E$ (GPa)	$\nu$	$\sigma_y$ (MPa)	$\rho$ (kg/m <sup>3</sup> )	$\alpha$ (10 <sup>-6</sup> K <sup>-1</sup> )	$\kappa_T$ (W/m K)	$c$ (J/kg K)
WC <sup>39</sup>	Pistons	645	0.21	420	15 500	7.1	88	240
ZrO <sub>2</sub> <sup>40</sup>	Anvils	250	0.28	500	5 680	8	2.3	460
Beryllco25 <sup>15,41</sup>	Gasket	119	0.3	900	8 250	17.3	84	418.7
Age-hardened Beryllco25	Locknuts/body	127	0.3	1380	8 290	17.3	84	418.7
Stycast epoxy 2850FT <sup>42</sup>	Needle	7.5	0.36	60	2 400	35	1.25	1000

space constrains, they have a typical diameter of 400  $\mu\text{m}$  and a length of 500  $\mu\text{m}$  and consist of about  $15 \pm 4$  windings. The Cu<sub>2</sub>O powder for the *in situ* pressure determination was embedded in paraffin wax and inserted inside the micro-coil. Finally, the bore of the gasket was filled with Daphne oil 7575,<sup>33</sup> suitable for experiments up to 4 GPa.<sup>34</sup> Considering the tiny dimensions of the anvil-cell components, the cell preparation operations had to be carried out under a microscope. For an enhanced precision, the use of micro-manipulators is highly recommended.

### B. Thermo-mechanical finite element analysis

To evaluate the deformation of the gasket, whose main purpose is to contain and compress the pressure transmitting medium, a comprehensive FEA of the cell was performed. In particular, the geometric model of the pressure cell was drafted using Autodesk Inventor<sup>35</sup> (see Fig. 2) and then discretized with ANSYS version 18.2<sup>36</sup> into 4-node brick elements

with an approximate mesh-grid size of 1 mm. Since the anvil indentation is expected to produce sharp stress variations, a finer mesh grid size of 0.1 mm was employed for modeling the gasket. A linear thermoelastic constitutive model<sup>37</sup> with temperature-dependent coefficients was assigned to each component, except for the gasket and anvils. Since the latter undergo plastic deformations during the experiments, an elasto-plastic constitutive model<sup>38</sup> was assigned to these two components. This model is characterized by the von Mises yield surface and isotropic hardening and assumes a post-yield tangent modulus equal to 1% of the corresponding elastic Young modulus. The material parameters reported in Table I for  $T = 293$  K and their slightly modified values at 10 K (see the caption of Table I) were employed to perform the thermomechanical analysis.

The pressure cell, including the main dimensions and boundary conditions, is shown schematically in Fig. 4. In order to simulate the clamping force of the locking thread after

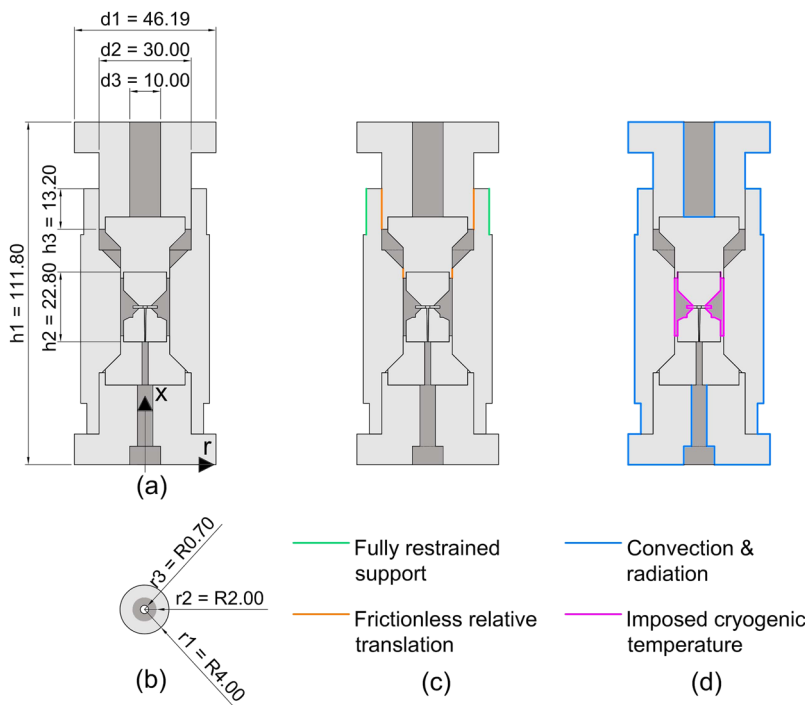


**FIG. 4.** (a) Longitudinal cross section of the pressure cell showing the main dimensions in a load-free condition:  $h_1$  is the total length;  $h_2$  is the distance between top and bottom surfaces of the anvils;  $h_3$  is the free sliding length between the upper locknut and the body, which are characterized by frictionless contact;  $d_1$  is the maximum external diameter of locknuts;  $d_2$  and  $d_3$  indicate locknut and pusher diameters. (b) Top view of the gasket with main dimensions (maximum size): for all the gasket sizes, the outer radius  $r_1$  is equal to 4 mm, whilst, for the largest gasket, the inner radius  $r_3$  is equal to 0.7 mm and the radius of the indented region  $r_2$  is equal to 2 mm. (c) Mechanical boundary conditions: the *fully restrained support* simulates the fixation of the pressure cell, constrained by a stiff aluminum cylinder (omitted in this picture); the *frictionless contact condition* allows for the relative translation of the upper locknut and body owing to piston pre-load. (d) Thermal boundary conditions: *convection and radiation* simulate heat exchange with the surroundings, whilst the *imposed cryogenic temperature* takes into account the effect of a heater-thermometer coupled system fixed on the outer surface of the body, close to the inspection hole, to enhance the control of the sample temperature. All the dimensions are in mm.

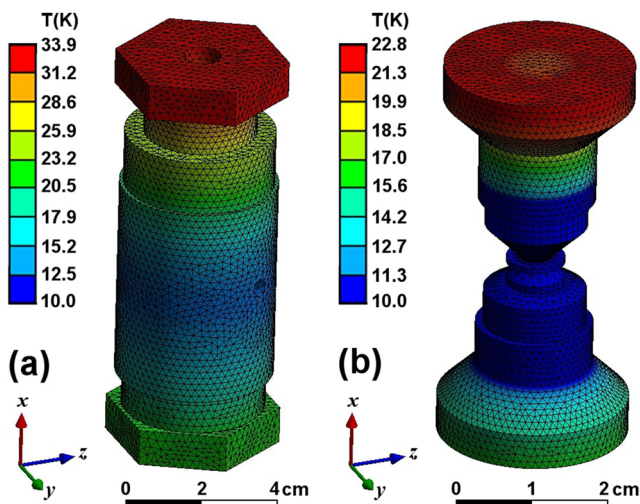


**FIG. 5.** Temperature distribution in (a) the body-nut system and (b) the piston-anvil-gasket system of the pressure cell, as resulting from thermal FEA at 10 K. The temperature in the sample area is rather uniform, reflecting the stabilizing action of the temperature controller. Elsewhere a gradient due to the upward helium flow is observed, not exceeding 10 K over the entire length of the pressure cell. The effect of temperature on the mechanical response of the cell is negligible.

preloading, corresponding to the cell configuration during measurements, the mating body and upper locknut surfaces were characterized by a frictionless contact, connected by a generalized linear spring oriented along the axial direction, and preloaded with a tensile force of 20 kN.

In order to simulate the heat exchange with the surroundings, convective and radiative boundary conditions were applied to the external surface of the pressure cell by considering a uniform convection coefficient of  $10 \text{ W/m}^2\text{K}$ .<sup>43</sup> Low-temperature conditions were simulated by imposing a uniform temperature of 10 K, regarded as a typical experimental scenario, on the inner cavity surface. The thermomechanical response of the cell to stress was evaluated in two steps. First, the stationary temperature distribution was computed

by solving the heat transfer equation across the whole volume of the cell, taking into account the thermal boundary condition presented in Fig. 4(d). Then, the thermal strains were recreated as equivalent mechanical loads during the mechanical FEA. In this regard, Fig. 5 provides an overview of the temperature distribution in the pressure cell. Figure 6 instead provides a close-up view of the mechanical response of the gasket at the end of the simulation.

The validity of the FEA calculations is confirmed by the plastic deformation of the gasket at the anvil contact region. Indeed, the calculated maximum indentation of about 0.17 mm [Fig. 6(a)] agrees well with the experimental value of 0.20 mm, measured with a scanning electron microscope (SEM) after applying pressure. We recall that, at the contact region, the equivalent von Mises stress exceeds the yield stress of the gasket (900 MPa), as presented in Fig. 6(c). The simulation assures also that the 0.4-mm wide RF micro-coil is not deformed during cell loading, provided it is correctly centered and the pressure is isotropic. In addition, simulations indicate also that higher pressures are likely to be achieved by employing composite gaskets, as previously reported.<sup>24</sup> In this case, defining the new geometric parameters and gasket properties should be sufficient to estimate the final higher pressure.

### III. *IN SITU* PRESSURE MEASUREMENTS VIA NQR

The NQR investigations included  $^{63}\text{Cu}$  (spin  $I = 3/2$ ) line shape measurements of  $\text{Cu}_2\text{O}$  before and after each cell-loading cycle, performed at 6 K (see Fig. 7). The zero-field signal was monitored by means of standard spin-echo sequences, consisting in  $\pi/2$  and  $\pi$  pulses of 2 and 4  $\mu\text{s}$ , respectively, with a recycle delay of 60 s. The NQR line shapes were obtained via fast Fourier Transform (FFT) of the echo signal which, due to the high sensitivity of the  $^{63}\text{Cu}$  nucleus, could be acquired using only 16 scans. In a detailed study,<sup>29</sup> H. Fukazawa *et al.* reported on the pressure-dependent<sup>44</sup> NQR frequency  $\nu_Q$  (MHz) of  $^{63}\text{Cu}$  in  $\text{Cu}_2\text{O}$  up to 10 GPa at 1.6 K. Here we use their calibration formula to determine the *in situ* pressure values,<sup>29</sup>

$$\nu_Q(p, T < 10 \text{ K}) = A + Bp + Cp^2, \quad (1)$$

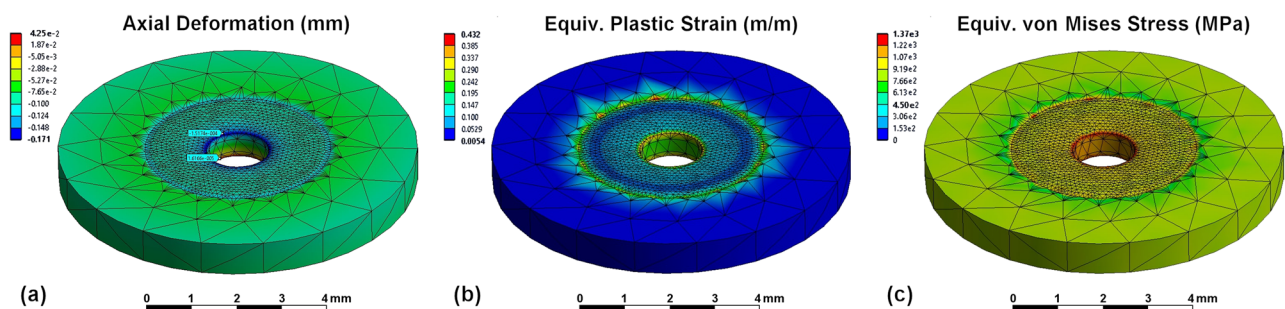


**FIG. 6.** Mechanical FEA of the gasket: (a) axial deformation; (b) equivalent plastic strain; (c) equivalent von Mises stress. FEA calculations predict an appreciable plastic deformation of the gasket at the anvil contact region, with an indentation of about 0.17 mm, very close to the experimentally measured value of 0.20 mm. At this location, the equivalent von Mises stress exceeds the yield stress of the gasket, here corresponding to 900 MPa.

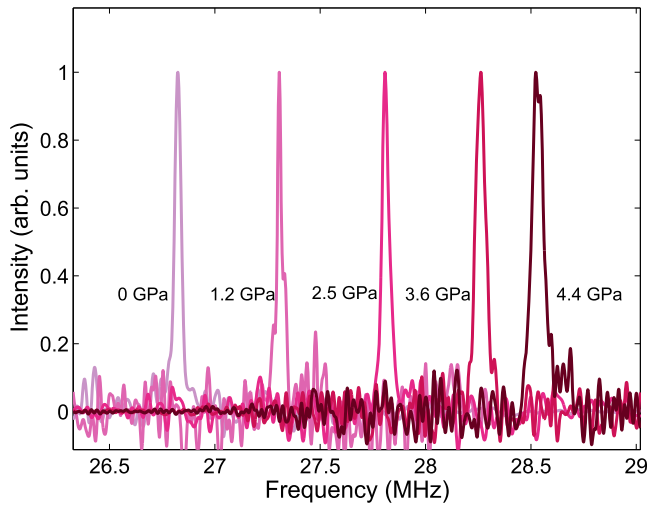


**FIG. 7.**  $^{63}\text{Cu}$  NQR signals in  $\text{Cu}_2\text{O}$  measured at 6 K in different applied pressures using a tapered feedthrough cell configuration. As expected, the NQR signal shifts toward higher frequencies upon increasing pressure. The pressure values were estimated by means of Eq. (1). Repeated measurements at 4.4 GPa indicate a persistent double-horn feature in correspondence with the peak maximum. Most likely this reflects a change in pressure character,<sup>15</sup> from hydrostatic to increasingly anisotropic between 3.6 and 4.4 GPa.

where  $p$  is measured in GPa, while  $A$ ,  $B$ , and  $C$  are 26.82, 0.3736, and  $-6.384 \times 10^{-4}$ , respectively. As indicated in Eq. (1), this analytical relation is valid below 10 K, where  $\nu_Q$  was shown to be temperature independent. At pressures above 10 GPa, a frequency saturation occurs. This formula represents a high-pressure extension of a previous relation<sup>28</sup> valid for pressures below 2 GPa and verified over a wide temperature range (from 4 to 300 K). This lower-pressure formula,<sup>28</sup>

$$\nu_Q(p, T < 10 \text{ K}) = 26.82 + 0.402p - 1.496 \times 10^{-4}p^2, \quad (2)$$

is similar to Eq. (1). The three parameters implicitly contain the temperature-dependence of  $\nu_Q$ , since they are proportional to the phonon distribution function  $\rho(T) = \coth(\hbar f_l / 2k_B T) / 2$ ,<sup>28</sup> according to the relations<sup>29</sup>

$$\begin{aligned} A(T) &= 27.06 - 0.4762\rho(T), \\ B(T) &= 0.4154 - 0.02682\rho(T), \\ C(T) &= -2.992 \times 10^{-4}\rho(T). \end{aligned} \quad (3)$$

Here  $h$  and  $k_B$  are the Planck and Boltzmann constants, respectively, while  $f_l$  is the low acoustic phonon frequency. In the harmonic approximation of the quantum theory of vibrations, one finds  $f_l = 2.82 \times 10^6$  MHz,<sup>45</sup> closely related to the vibration frequency of Cu–O–Cu bonds. The latter provide the dominant contribution to the electric field gradient (EFG) tensor<sup>45</sup>  $V_{ij} = \partial^2 V / \partial x_i \partial x_j$ , where  $V(\mathbf{r})$  is the electrostatic potential generated by the charge distribution of electrons and nuclei. Conceptually the  $p$ -dependence of the quadrupole resonance  $\nu_Q$  can also be explained by assuming the validity of the point-charge model, a good approximation for the  $\text{Cu}_2\text{O}$  system. Under this assumption, the electric quadrupole

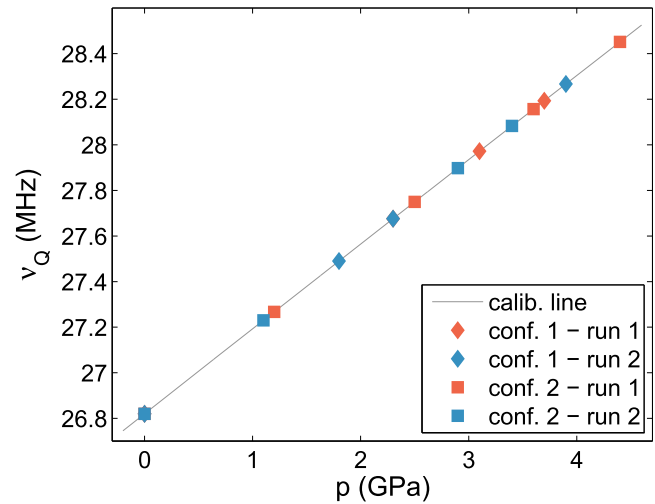


**FIG. 8.**  $^{63}\text{Cu}$  NQR resonance frequency in  $\text{Cu}_2\text{O}$  vs. pressure, measured at 6 K. Pressure was determined by means of the calibration equation (1), gray line. Diamonds and squares indicate data obtained by using the first and second configuration, respectively. Colors refer to the different run numbers.

Hamiltonian is proportional to the  $V_{zz}$  term of the EFG tensor, in turn proportional to the inverse of the unit cell volume  $v_c$ .<sup>29</sup> Consequently, apart from minor corrections due to hybridization effects,  $\nu_Q \propto p$  since<sup>29</sup>

$$\frac{v_c^0}{v_c^p} = \left(1 + \frac{B_1}{B_0} p\right)^{1/B_1}, \quad (4)$$

where  $v_c^0$  and  $v_c^p$  are the unit cell volumes of  $\text{Cu}_2\text{O}$  at zero and under applied pressure (in GPa), while  $B_0 = 131$  GPa and  $B_1 = 5.7$  are the zero-pressure bulk modulus and its derivative, respectively.<sup>46</sup>

The data shown in Figs. 7 and 8 were obtained by using the hybrid cell in the second configuration, which comprises a feedthrough in the bottom anvil, a  $\varnothing 1.2$ -mm indenter, and a gasket with a small hole (0.4 mm), the latter allowing us to achieve higher pressure values. Compatible results were obtained also by using the first configuration (where the coil leads are in contact with gold electrodes). We recall that 4.4 GPa is the highest pressure achieved; pressures up to about 4 GPa can be achieved routinely. Besides the  $\text{Cu}_2\text{O}$  test case, the hybrid cell in the second configuration (i.e., lower anvil with the feedthrough) was used also in real-case scenarios, as, e.g., to measure the pressure-dependent  $^{23}\text{Na}$  NMR signal in the  $\text{Na}_2\text{IrO}_3$  honeycomb iridate,<sup>10</sup> a candidate quantum-spin-liquid material.

#### IV. CONCLUSION

We have successfully designed, produced, and tested a new hybrid piston-clamped anvil cell, suitable for nuclear-magnetic-resonance measurements up to 4.4 GPa. The adopted finite-element analysis proved to be successful in describing the thermomechanical response of the cell in

typical experimental conditions. This approach, able to predict the thermo-mechanical behavior of complex systems, represents an effective way to optimize the design of similar devices. From this perspective, we prioritized here an efficient design and thermo-mechanical simulation protocol to the possibility of reaching very high pressures. In particular, our model predicts accurately the plastic deformation (i.e., indentation) of the gasket, thus offering a guideline for future designs which may employ composite gaskets to achieve higher pressures with no or minor deformations of the coil. The pressure was monitored *in situ* by means of  $^{63}\text{Cu}$  NQR in  $\text{Cu}_2\text{O}$ . Compared to the ruby-fluorescence technique, this method offers the advantage of admitting anvils made of any hard material (typically  $\text{ZrO}_2$ ), thus dropping the constraint of optical transparency, which imposes the use of diamond anvils.

Our design combines the advantages of piston-clamped systems, i.e., robustness and handiness, with those of anvil cells, which allows us to achieve higher pressures. The reported solution admittedly has its weaknesses, including the delicate loading of the cell due to the small size of the inner components, the fragility of the coil, and the connecting leads. To overcome these limitations and achieve higher pressures, above we provide hints for the development of improved systems. These include the reduction of the indenting diameter of the anvil, the use of composite gaskets, and the use of more advanced techniques for centering and fixing the gasket.

## ACKNOWLEDGMENTS

The authors thank M. Elender, S. Holenstein, M. Horisberger, R. Khasanov, Z. Shermadini, and T. Strässle for useful discussions and help. This work was financially supported in part by the Schweizerische Nationalfonds zur Förderung der Wissenschaftlichen Forschung through Grant No. 200021-169455.

## REFERENCES

- 1 P. F. McMillan, "New materials from high-pressure experiments," *Nat. Mater.* **1**, 19–25 (2002).
- 2 J. Wittig, "Superconductivity of cerium under pressure," *Phys. Rev. Lett.* **21**, 1250–1252 (1968).
- 3 J.-G. Cheng, K. Matsubayashi, W. Wu, J. P. Sun, F. K. Lin, J. L. Luo, and Y. Uwatoko, "Pressure induced superconductivity on the border of magnetic order in MnP," *Phys. Rev. Lett.* **114**, 117001 (2015).
- 4 J. Chaloupka, G. Jackeli, and G. Khaliullin, "Kitaev-Heisenberg model on a honeycomb lattice: Possible exotic phases in iridium oxides  $\text{A}_2\text{IrO}_3$ ," *Phys. Rev. Lett.* **105**, 027204 (2010).
- 5 J. Chaloupka, G. Jackeli, and G. Khaliullin, "Zigzag magnetic order in the iridium oxide  $\text{Na}_2\text{IrO}_3$ ," *Phys. Rev. Lett.* **110**, 097204 (2013).
- 6 J. Chaloupka and G. Khaliullin, "Hidden symmetries of the extended Kitaev-Heisenberg model: Implications for the honeycomb-lattice iridates  $\text{A}_2\text{IrO}_3$ ," *Phys. Rev. B* **92**, 024413 (2015).
- 7 A. Banerjee, C. A. Bridges, J.-Q. Yan, A. A. Aczel, L. Li, M. B. Stone, G. E. Granroth, M. D. Lumsden, Y. Yiu, J. Knolle, S. Bhattacharjee, D. L. Kovrizhin, R. Moessner, D. A. Tennant, D. G. Mandrus, and S. E. Nagler, "Proximate Kitaev quantum spin liquid behaviour in a honeycomb magnet," *Nat. Mater.* **15**, 733–740 (2016).
- 8 V. Hermann, M. Altmeyer, J. Ebad-Allah, F. Freund, A. Jesche, A. A. Tsirlin, M. Hanfland, P. Gegenwart, I. I. Mazin, D. I. Khomskii, R. Valentí, and C. A. Kuntscher, "Competition between spin-orbit coupling, magnetism, and dimerization in the honeycomb iridates:  $\alpha$ - $\text{Li}_2\text{IrO}_3$  under pressure," *Phys. Rev. B* **97**, 020104(R) (2018).
- 9 M. Majumder, R. S. Manna, G. Simutis, J. C. Orain, T. Dey, F. Freund, A. Jesche, R. Khasanov, P. K. Biswas, E. Bykova, N. Dubrovinskaia, L. S. Dubrovinsky, R. Yadav, L. Hozoi, S. Nishimoto, A. A. Tsirlin, and P. Gegenwart, "Breakdown of magnetic order in the pressurized Kitaev iridate  $\beta$ - $\text{Li}_2\text{IrO}_3$ ," *Phys. Rev. Lett.* **120**, 237202 (2018).
- 10 G. Simutis, N. Barbero, K. Rolfs, P. Leroy-Calatayud, K. Mehlatat, R. Khasanov, H. Luetkens, E. Pomjakushina, Y. Singh, H.-R. Ott, J. Mesot, A. Amato, and T. Shiroka, "Chemical and hydrostatic-pressure effects on the Kitaev honeycomb material  $\text{Na}_2\text{IrO}_3$ ," *Phys. Rev. B* **98**, 104421 (2018).
- 11 A. P. Drozdov, M. I. Erements, I. A. Troyan, V. Ksenofontov, and S. I. Shylin, "Conventional superconductivity at 203 kelvin at high pressures in the sulfur hydride system," *Nature* **525**, 73–76 (2015).
- 12 H. Liu, I. I. Naumov, R. Hoffmann, N. W. Ashcroft, and R. J. Hemley, "Potential high- $T_c$  superconducting lanthanum and yttrium hydrides at high pressure," *Proc. Natl. Acad. Sci. U. S. A.* **114**, 6990–6995 (2017).
- 13 A. P. Drozdov, V. S. Minkov, S. P. Besedin, P. P. Kong, M. A. Kuzovnikov, D. A. Knyazev, and M. I. Erements, "Superconductivity at 215 K in lanthanum hydride at high pressures," e-print [arXiv:1808.07039](https://arxiv.org/abs/1808.07039) (2018).
- 14 D. K. Bradley, J. H. Eggert, R. F. Smith, S. T. Prisbrey, D. G. Hicks, D. G. Braun, J. Biener, A. V. Hamza, R. E. Rudd, and G. W. Collins, "Diamond at 800 GPa," *Phys. Rev. Lett.* **102**, 075503 (2009).
- 15 M. I. Erements, *High Pressure Experimental Methods* (Oxford University Press, Oxford, 1996).
- 16 N. Fujiwara, "Fabrication and efficiency evaluation of a hybrid NiCrAl pressure cell up to 4 GPa," *Rev. Sci. Instrum.* **78**, 073905 (2007).
- 17 P. W. Bridgman, "The measurement of high hydrostatic pressure. I. A simple primary gauge," *Proc. Am. Acad. Arts Sci.* **44**, 201–217 (1909).
- 18 R. L. Reichlin, "Measuring the electrical resistance of metals to 40 GPa in the diamond-anvil cell," *Rev. Sci. Instrum.* **54**, 1674–1677 (1983).
- 19 S.-H. Lee, K. Luszczynski, R. E. Norberg, and M. S. Conradi, "NMR in a diamond anvil cell," *Rev. Sci. Instrum.* **58**, 415–417 (1987).
- 20 R. Bertani, M. Mali, J. Roos, and D. Brinkmann, "A diamond anvil cell for high-pressure NMR investigations," *Rev. Sci. Instrum.* **63**, 3303–3306 (1992).
- 21 K. Kitagawa, H. Gotou, T. Yagi, A. Yamada, T. Matsumoto, Y. Uwatoko, and M. Takigawa, "Space efficient opposed-anvil high-pressure cell and its application to optical and NMR measurements up to 9 GPa," *J. Phys. Soc. Jpn.* **79**, 024001 (2010).
- 22 M. Itoh, "Recent development of high-pressure NMR and NQR experiments up to 10 GPa," *JPSJ News Comments* **7**, 03 (2010).
- 23 K. Kitagawa, H. Gotou, T. Yagi, A. Yamada, T. Matsumoto, Y. Uwatoko, and M. Takigawa, "10 GPa-class high-pressure NMR technique realized by the new cell with improved space efficiency," *Rev. High Pressure Sci. Technol.* **22**, 198–205 (2012).
- 24 T. Meier and J. Haase, "Anvil cell gasket design for high pressure nuclear magnetic resonance experiments beyond 30 GPa," *Rev. Sci. Instrum.* **86**, 123906 (2015).
- 25 T. Meier, S. Reichardt, and J. Haase, "High-sensitivity NMR beyond 200 000 atmospheres of pressure," *J. Magn. Reson.* **257**, 39–44 (2015).
- 26 T. Meier, S. Khandarkhaeva, S. Petitgirard, T. Körber, A. Lauerer, E. Rössler, and L. Dubrovinsky, "NMR at pressures up to 90 GPa," *J. Magn. Reson.* **292**, 44–47 (2018).
- 27 A. D. Chijioke, W. J. Nellis, A. Soldatov, and I. F. Silvera, "The ruby pressure standard to 150 GPa," *J. Appl. Phys.* **98**, 114905 (2005).
- 28 A. P. Reyes, E. T. Ahrens, R. H. Heffner, P. C. Hammel, and J. D. Thompson, "Cuprous oxide manometer for high pressure magnetic resonance experiments," *Rev. Sci. Instrum.* **63**, 3120–3122 (1992).
- 29 H. Fukazawa, N. Yamatoji, Y. Kohori, C. Terakura, N. Takeshita, Y. Tokura, and H. Takagi, "Manometer extension for high pressure measurements: Nuclear quadrupole resonance study of  $\text{Cu}_2\text{O}$  with a modified Bridgman anvil cell up to 10 GPa," *Rev. Sci. Instrum.* **78**, 015106 (2007).

- <sup>30</sup>See <https://www.almax-easylab.com/TypeIIacBoehlerAlmaxdesign.aspx> for “DAC Boehler-Almax design”; accessed 03 September 2018.
- <sup>31</sup>Y. Miyakawa, “Friction and wear performance of gold and gold alloy films,” *Gold Bull.* **13**, 21–30 (1980).
- <sup>32</sup>L. G. Steele, M. Lawson, M. Onyszczak, B. T. Bush, Z. Mei, A. P. Dioguardi, J. King, A. Parker, A. Pines, S. T. Weir, W. Evans, K. Visbeck, Y. K. Vohra, and N. J. Curro, “Optically detected magnetic resonance of nitrogen vacancies in a diamond anvil cell using designer diamond anvils,” *Appl. Phys. Lett.* **111**, 221903 (2017).
- <sup>33</sup>N. Tateiwa and Y. Haga, “Evaluations of pressure-transmitting media for cryogenic experiments with diamond anvil cell,” *Rev. Sci. Instrum.* **80**, 123901 (2009).
- <sup>34</sup>R. Khasanov, Z. Guguchia, A. Maisuradze, D. Andreica, M. Elender, A. Raselli, Z. Shermadini, T. Goko, F. Knecht, E. Morenzoni, and A. Amato, “High pressure research using muons at the Paul Scherrer Institute,” *High Pressure Res.* **36**, 140–166 (2016).
- <sup>35</sup>Autodesk, Inc., “Autodesk Inventor,” 2018.
- <sup>36</sup>Ansys, Inc., “ANSYS Academic Research Mechanical,” 2017.
- <sup>37</sup>H. Ziegler, *An Introduction to Thermomechanics*, North-Holland Series in Applied Mathematics and Mechanics, 2nd ed. (North-Holland, Amsterdam, 1983), Vol. 21.
- <sup>38</sup>E. de Souza Neto, D. Peric, and D. Owens, *Computational Methods for Plasticity: Theory and Applications* (John Wiley & Sons, Chichester, 2008).
- <sup>39</sup>A. S. Kurlov and A. I. Gusev, *Tungsten Carbides: Structure, Properties and Application in Hardmetals*, Springer Series in Materials Science (Springer International Publishing, Switzerland, 2013), Vol. 184.
- <sup>40</sup>ZrO<sub>2</sub>: Round profile datasheet, Morgan Technical Ceramics, Australia, 2017.
- <sup>41</sup>EN 12163:12167, European Committee for Standardization, 2018, BeCu: datasheets.
- <sup>42</sup>Stycast epoxy 2850FT: datasheet, Emerson & Cuming Microwave Products, Inc., USA, 2015.
- <sup>43</sup>*Heat Transfer Handbook*, edited by A. Bejan and A. D. Kraus (John Wiley & Sons, Hoboken, NJ, 2003).
- <sup>44</sup>F. D. Murnaghan, *Finite Deformation of an Elastic Solid* (Wiley, New York, 1951).
- <sup>45</sup>H. Bayer, “Zur theorie der spin-gitterrelaxation in molekülkristallen,” *Z. Phys.* **130**, 227–238 (1951).
- <sup>46</sup>A. Werner and H. D. Hochheimer, “High-pressure x-ray study of Cu<sub>2</sub>O and Ag<sub>2</sub>O,” *Phys. Rev. B* **25**, 5929–5934 (1982).